



What can we see with IVIM MRI?

Denis Le Bihan

NeuroSpin, Frédéric Joliot Institute, Bât 145, CEA-Saclay Center, Gif-sur-Yvette, 91191 France

ARTICLE INFO

Keywords:

MRI
IVIM
Perfusion
Diffusion
Functional MRI
Blood flow
Blood volume
Mean transit time

ABSTRACT

Intravoxel Incoherent Motion (IVIM) refers to translational movements which within a given voxel and during the measurement time present a distribution of speeds in orientation and/or amplitude. The IVIM concept has been used to estimate perfusion in tissues as blood flow in randomly oriented capillaries mimics a pseudo-diffusion process. IVIM-based perfusion MRI, which does not require contrast agents, has gained momentum recently, especially in the field oncology. In this introductory review the basic concepts, models, technical requirements and limitations inherent to IVIM-based perfusion MRI are outlined, as well as new, non-perfusion applications of IVIM MRI, such as virtual MR Elastography.

“Intravoxel Incoherent Motion (IVIM) refers to translational movements which within a given voxel and during the measurement time present a distribution of speeds in orientation and/or amplitude” (Le Bihan et al., 1986, 1988; Le Bihan, 1990). The concept was introduced in 1986 together with the foundation of Diffusion MRI (Le Bihan et al., 1986), as it was realized that flow of blood in capillaries (perfusion) would mimic a diffusion process and impact diffusion MRI measurements. Soon after it was shown how perfusion and diffusion effects can be disentangled in diffusion MRI, leading to separate maps and measurements of molecular diffusion and perfusion (Le Bihan et al., 1988). As a side effect of this view “diffusion MRI” and “perfusion MRI” have been associated for many years in the MR imaging and radiology communities where “diffusion and perfusion MRI” often appeared as session titles or journal keywords. Indeed, IVIM MRI is experiencing a remarkable revival for applications throughout the body, especially for oncologic applications, as IVIM MRI does not involve contrast agents. Still, per its definition IVIM does not specifically refer to blood microcirculation, as other sources of intravoxel incoherent motion are possible, as will be highlighted in this article. Reviews on the clinical potential IVIM MRI have been published elsewhere and the scope of this topical review which has an educational content is rather to introduce the concepts behind IVIM MRI, related methodological issues, and present future directions, both in terms of technical developments and application fields.

The IVIM concept

IVIM MRI has its roots in diffusion MRI. Diffusion refers to the

random movement of *individual* molecules (most often water for diffusion MRI). Due to their thermal energy all molecules move, colliding against each other. Each collision results in a change in the motion direction of each molecule, and the overall process is well described by a random walk, as first realized by Einstein. For liquid water the average of *individual* molecular displacement between two “collisions”, l , in three-dimensional space, is in the 10th of a nanometer range while mean “velocity” (a concept more valid for a gas phase than a liquid phase), v , is around 100 m/s, which correspond to a diffusion coefficient, D , around $10^{-9} \text{ m}^2/\text{s}$ based on Einstein equation ($D = lv/6$). On a statistical basis, taking into account billions of molecules, each one diffusing on its own, this movement translates into an overall displacement along one spatial direction which obey a Gaussian distribution with a width of $17 \mu\text{m}$ during a time interval of 50 ms, a perfect scale to explore the microstructure of biological tissues in vivo (Fig. 1). In the framework of diffusion MRI this random displacement of *individual* molecules results in a signal attenuation in the presence of magnetic field encoding gradient pulses. This attenuation increases with the diffusion coefficient and the degree of sensitization to diffusion of the MRI pulse sequence (so called b value), taking the form of a monoexponential decay with the b value (Le Bihan et al., 1986).

While diffusion and blood microcirculation are two completely different physical phenomena taking place at very different spatial and temporal scales, apparent motion randomness can be seen, instead, in the geometry of the vessel network where blood circulates. In other word, randomness results from the *collective* motion of blood water molecules in the network, flowing from one capillary segment to the next. This

E-mail address: denis.lebihan@gmail.com.

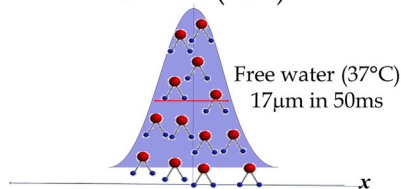
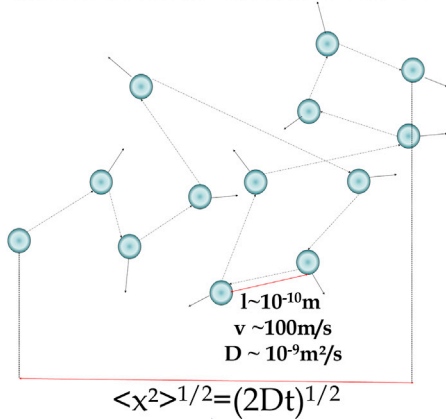
<https://doi.org/10.1016/j.neuroimage.2017.12.062>

Received 2 September 2017; Received in revised form 28 November 2017; Accepted 19 December 2017

Available online 22 December 2017

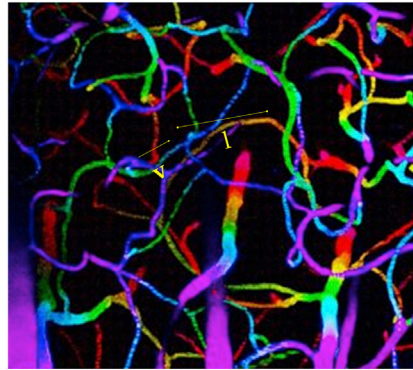
1053-8119/© 2018 The Author. Published by Elsevier Inc. This is an open access article under the CC BY-NC-ND license (<http://creativecommons.org/licenses/by-nc-nd/4.0/>).

Individual water molecular diffusion



Molecular diffusion

Blood pool collective water flow



$l \sim 10^{-4} \text{ m}$
 $v \sim 1 \text{ mm/s}$
 $D^* \sim 10^{-8} \text{ m}^2/\text{s}$

Blood microcirculation (pseudo-diffusion)

collective movement may be viewed as a *pseudodiffusion* process where average displacements, l , would now correspond to the mean capillary segment length and the mean velocity, v , would be that of blood in the vessels (Fig. 1). Extending Einstein's diffusion equation to pseudodiffusion provides a value for the pseudo-diffusion coefficient, $D^* = lv/6$, which is around $10^{-8} \text{ m}^2/\text{s}$ taking for l 100 μm and for v 1 mm/s. This is

where luck strikes: D^* is close enough to D , which means that diffusion MRI is sensitive to both diffusion and blood microcirculation, both resulting, separately, in a monoexponential decay of the MRI signal with the b value. However, the blood microcirculation component decays 10 times faster, which allows the two independent phenomena to be separated. Interestingly, the value for D^* is found similar across other species

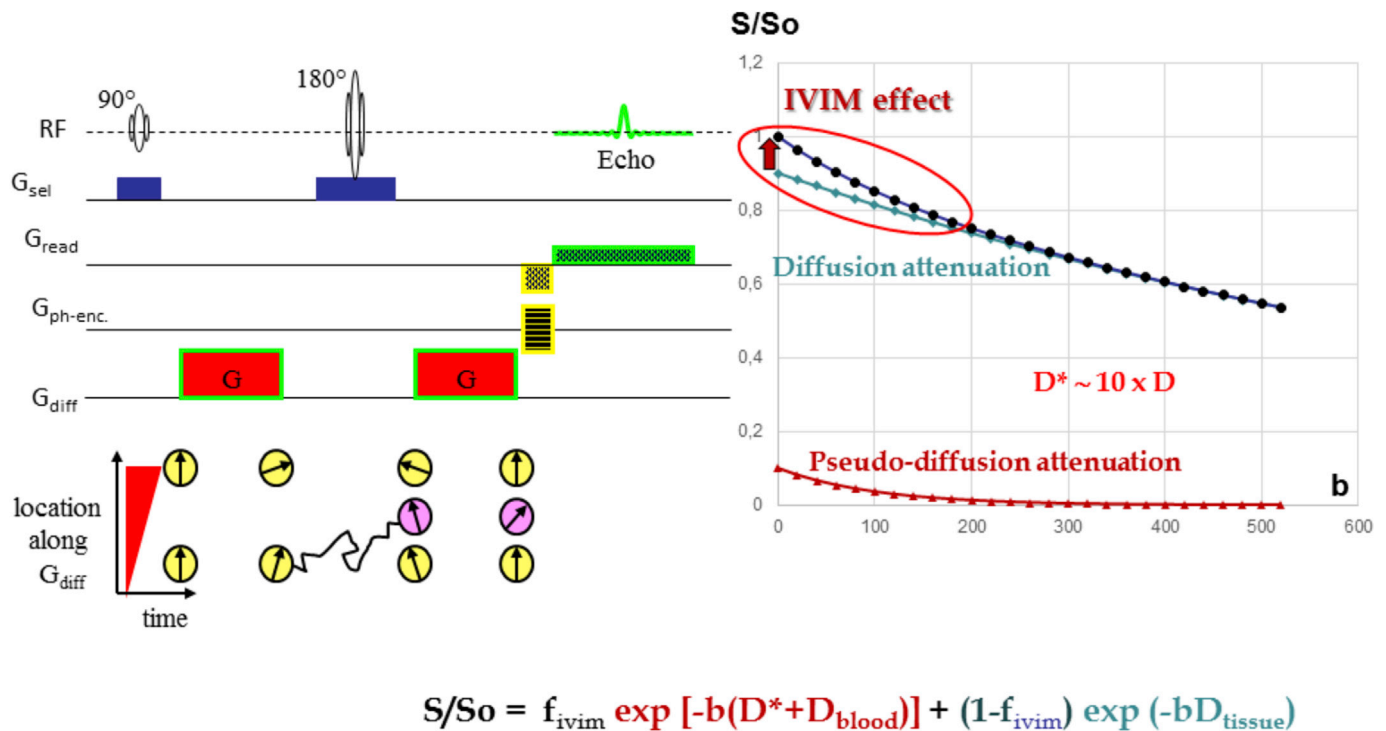


Fig. 2. Effects of diffusion and pseudo-diffusion on the MRI signal.

Random water displacements (either from individual molecular motion or from collective water incoherent flow at voxel level) results in a exponential decay of the signal amplitude with the degree of field gradient encoding (b value). The tissue diffusion and blood flow component contribute separately to the signal, resulting to a biexponential shape. However, as $D^* \gg D$ the IVIM (blood flow) effect appears as a deviation of the tissue diffusion signal decay at low b values.

which have been scanned (Fournet et al., 2017), which is not completely surprising as small animals have shorter capillary segments, but higher flow velocities (Pavlik et al., 1981).

The overall MRI signal attenuation, S/S_0 , is simply the sum of the tissue and blood components (assuming water exchange between blood and tissues is negligible during the encoding time, a hypothesis which still needs to be investigated), taking the shape of a biexponential decay:

$$S/S_0 = f_{\text{IVIM}} \exp[-b(D^* + D_{\text{blood}})] + (1 - f_{\text{IVIM}}) \exp(-bD) \quad [1]$$

where f_{IVIM} is the flowing blood fraction, D is the water diffusion coefficient in the tissue and D_{blood} the water diffusion coefficient in blood (diffusion of individual water molecules in blood obviously occurs in addition to the blood circulation driven IVIM effect). However, given the small fraction of the flowing blood (a few %) compared to the overall tissue water content, the perfusion driven IVIM signature appears more as a deviation as small b values of the tissue diffusion driven mono-exponential signal decay (Fig. 2).

From the early days of IVIM MRI to contemporary perfusion MRI

At small b -values, both diffusion and flowing blood effects are present and the Apparent Diffusion Coefficient, ADC (Le Bihan et al., 1986), calculated from signals $S(b)$ and $S(0)$ as $\ln[S(b)/S(0)]/b$ is higher than when using larger values. As f_{IVIM} is usually small, one has $\text{ADC} \sim D + f_{\text{IVIM}}/b$, and f_{IVIM} simply appears as the (negative) intercept of the diffusion component of the signal decay in log plots with b values (Fig. 3) (Le Bihan et al., 1988). Indeed, the first perfusion-driven IVIM measurements were obtained using 3 b values (0, 100 and 200 s/mm^2 , the highest achievable value with the hardware available at that time) (Le Bihan et al., 1988) (Fig. 3). The concept was first validated in a dedicated phantom (Fig. 6 in (Le Bihan et al., 1988)) made of packed calibrated

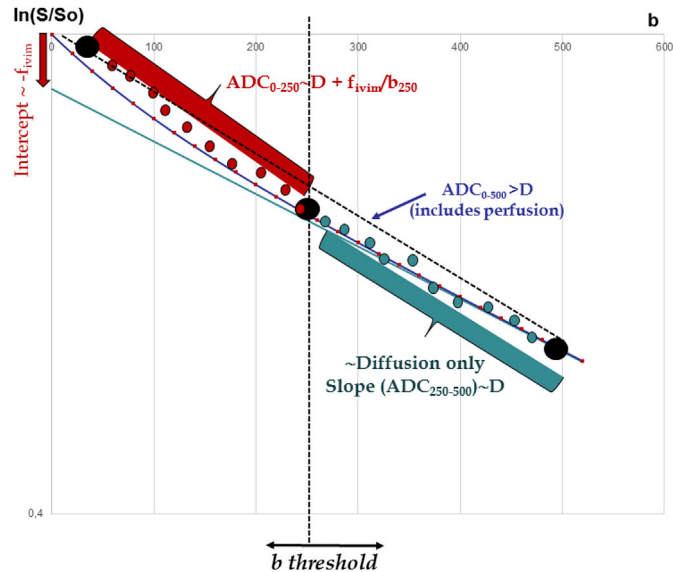


Fig. 3. Strategies to process IVIM/diffusion data sets.

Above a given threshold (which depends on the tissue IVIM/diffusion intrinsic parameters) for the b values only tissue diffusion contributes to the signal decay. The ADC obtained with b values higher than this threshold (eg. $\text{ADC}_{250-500}$) is the tissue diffusion coefficient, D . At lower b values (eg. ADC_{0-250}) the ADC includes the blood flow component. Hence, the flowing blood fraction (f_{IVIM} , which is the intercept of the tissue diffusion decay curve) can be obtained from those 2 ADC values, that is only 3 b values in total. Alternately, one may prefer fitting the overall signal attenuation curve with a IVIM/diffusion model. To reduce the effect of noise, one often performs fitting in 2 steps, first estimating diffusion from high b values signals, then subtracting the tissue diffusion component from the overall signal to estimate the IVIM parameters.

sephadex beads, inside which water could diffuse and between which a flow of water was maintained, mimicking random flow in capillaries, and in a small series of patients with tumors. The idea to get perfusion images from diffusion MRI, without the need for tracers or contrast agents, was found ground-breaking at the time (Dixon, 1988). Unfortunately, with the conventional 2DFT spin-echo sequences then available the acquisition time was about 10 min per b value and huge motion artifacts were often present in the images, so the IVIM method appeared controversial, although several groups validated the concept (Powers et al., 1991; Morvan, 1995; Pickens et al., 1992; Neil et al., 1994). IVIM became available in the clinical world after its coupling with echo-planar imaging (EPI), as signal acquired at multiple and higher b values could be obtained free of motion artifacts (Turner et al., 1990), allowing the first clinical validation of IVIM perfusion MRI in a series of patients with liver lesions (Yamada et al., 1999).

An early goal of IVIM MRI was to produce maps of brain perfusion to investigate brain function, given the known coupling between neural activation, metabolism, and blood flow. It did not work very well due to the technical limitations of early MRI scanners and IVIM-based fMRI did not survive competing methods that appeared at about the same time, one based on contrast agents (Belliveau et al., 1991) and short-lived and the other based on the blood oxygen level dependent (BOLD) concept (Ogawa et al., 1992). BOLD was clearly much easier to implement and much more sensitive for fMRI. Later work, however, has proven the validity of the IVIM concept, with an increase in the IVIM perfusion parameters in brain activated regions, and the potential of the approach to aid in our understanding of the different vascular contributions to the fMRI signal (Song et al., 1996; Truong and Song, 2009) (Fig. 4). Interestingly, IVIM MRI has also been used in the context of fMRI, however in a corrective way to remove blood flow effects in medium-sized vessels. A limitation of BOLD fMRI is its spatial resolution, as flow increases in somewhat large arteries or veins feed or drain large neuronal territories. By inserting “IVIM” gradient pulses in the MRI sequence (corresponding to low b -values), one may crush the contribution of the largest vessels (with high D^* values associated with fast flow) in the BOLD signal and improve the spatial resolution of the activation maps (Jin et al., 2006; Boxerman et al., 1995; Lee et al., 2002; Duong et al., 2003; Song and Li, 2003; Michelich et al., 2006). Several groups have relied on this trick, though not always considering referring to the IVIM concept. This IVIM concept has also been borrowed to improve other applications, for instance, arterial spin labeling (ASL) (Silva et al., 1997; Kim and Kim, 2006), or to suppress signal from extracellular flowing fluid in perfused cell systems (Van Zijl et al., 1991).

Today, the most promising clinical application for IVIM perfusion MRI is, however, oncology (Fig. 4). Many articles have been published and an extensive review is out of the scope of this introduction (see, for instance, Koh et al., 2011; Iima and Le Bihan, 2016). Perfusion imaging, such as IVIM MRI, is an important diagnostic imaging modality to evaluate neoangiogenesis or microvasculature heterogeneity, as well as to monitor treatment efficacy of chemo- or radiotherapy, and especially the effectiveness of antiangiogenic drugs or vascular targeting agents. Beside brain and head tumors (Federau et al., 2014; Kim et al., 2014; Bisdas et al., 2013; Fujima et al., 2014) perfusion-driven IVIM MRI is currently being investigated to assess malignant lesions in the prostate (Döpfert et al., 2011) and the breast (Sigmund et al., 2011; Bokacheva et al., 2014; Iima et al., 2015, 2017).

In the liver Yamada et al. (1999) showed the potential of IVIM MRI to differentiate HCC (hepatocellular carcinoma), hemangioma and cysts. Several studies have shown the potential of IVIM MRI for the evaluation of liver cirrhosis (Luciani et al., 2008) or fibrosis (Patel et al., 2010; Chow et al., 2012), as well as for the tissue characterization of focal liver lesions (Ichikawa et al., 2013a; Andreou et al., 2013; Yoon et al., 2014). The IVIM perfusion fraction has been shown as a potential biomarker of NASH (nonalcoholic steatohepatitis) (Joo et al., 2014; Van Beers, 2014). Still, IVIM/diffusion MRI for assessing hepatic lesions is challenging, as there is sometimes an overlap between benign and malignant lesions and

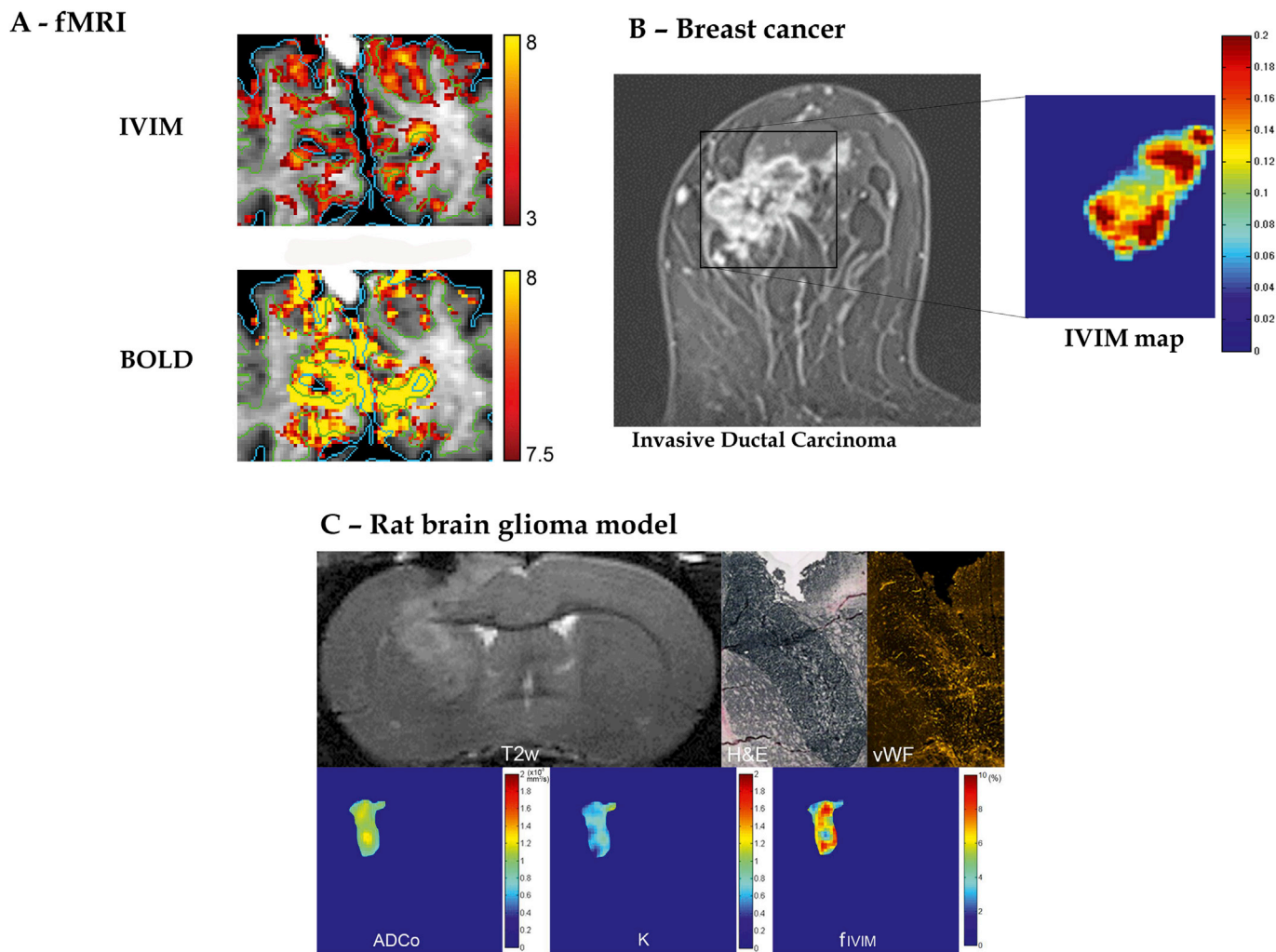


Fig. 4. Applications of perfusion-driven IVIM MRI.

A- The increase in blood flow/volume occurring in activated brain areas can be detected and mapped with IVIM MRI. The sensitivity of IVIM MRI to noise, however, makes this approach less robust than standard BOLD fMRI. IVIM fMRI, though, may provide a higher resolution than BOLD fMRI as it is sensitive to flow in smaller vessels (from [Truong and Song, 2009](#)).

B- Maps of fIVIM (flowing blood volume fraction) in malignant tissues (here a breast Invasive Ductal Carcinoma) highlight areas with high perfusion, likely the most active parts of the tumor signaling targets for biopsies (from [Iima et al., 2013](#)).

C- The fIVIM map obtained in a rat brain glioma model shows additional information to that conveyed by ADCo and Kurtosis maps. Areas with high fIVIM values colocalize with areas rich in small vessels, as authenticated by histology (vWF marking) (from [Iima et al., 2014](#)).

normal liver tissue ([Anderson et al., 2014](#); [Taouli et al., 2003](#); [Koh et al., 2006](#)). Besides, IVIM and diffusion MRIs in the liver is degraded by artifacts due to cardiac and respiratory motion ([Lee et al., 2015](#); [Dyvorne et al., 2013](#)) or to air in the adjacent stomach or colon.

In the kidneys IVIM parameters seem to be more useful than diffusion parameters with the potential to predict the extent of deterioration in renal function ([Ichikawa et al., 2013b](#)): D^* in the renal cortex is significantly lower in both mild and severe renal dysfunction, while ADC values drop only in severe renal dysfunction. The perfusion fraction, fIVIM, and the tissue diffusivity have shown better diagnostic performance, separately, than the overall ADC for the discrimination of enhancing from non-enhancing renal lesions, with a good correlation between fIVIM and perfusion-related parameters using gadolinium-based contrast agents ([Chandarana et al., 2011](#)). Furthermore, histogram analyses of IVIM data have been shown useful for the discrimination of malignant and benign tumors, as well as renal tumor subtypes ([Chandarana et al., 2012](#); [Gaing et al., 2015](#)).

Indeed, IVIM MRI is experiencing a remarkable revival for applications throughout the body. The first reason is certainly that vast progress has been made in MRI scanner hardware and sequence developments,

satisfying the signal:noise ratio hungry IVIM method. The second reason is that diffusion MRI has become a pillar of clinical MRI, part of many protocols, so that one may get IVIM/perfusion images “for free” together with the diffusion images, without the need for additional scanning time. The third reason is that IVIM MRI does not involve contrast agents, serving as an interesting alternative to perfusion MRI in some patients with contraindications for contrast agents, such as patients with renal failure at risk for Nephrogenic Systemic Fibrosis (NSF). Recently, an accumulation of gadolinium deposits in the brain or other organs in patients having received multiple injections of contrast agents has been demonstrated ([Kanda et al., 2014, 2015](#)). The IVIM method, thus, appears particularly appealing for patients requiring multiple MRI scans (oncology), as well as for children or pregnant patients.

Practical considerations for IVIM perfusion MRI

Data acquisition and processing scheme: 3- b values versus multiple b values

The 3 b values scheme used at the beginning of IVIM MRI ([Fig. 3](#)) has gained popularity recently although larger gradient strengths available,

as this approaches minimizes acquisition times. If one considers that IVIM effects have disappeared for b values above $250 \text{ mm}^2/\text{s}$ the slope of the signal attenuation between $b = 250$ and, say, 600 s/mm^2 is, according to Eq. (1), just the tissue diffusion coefficient D : $\text{ADC}_{250-600} \sim D$, while $\text{ADC}_{0-250} \sim D + f_{\text{IVIM}}/250$. The perfusion fraction then comes as $250 \times (\text{ADC}_{0-250} - \text{ADC}_{250-600})$, where the ADC is defined as:

$$\text{ADC}_{b_i-b_j} = \ln[S(b_i)/S(b_j)]/(b_j - b_i) \quad [2]$$

The problem with this simple approach is, first, that D^* cannot be estimated and second that the estimation of IVIM and diffusion parameters may be noisy. A solution to the second issue is to acquire multiple signals at those $3b$ values and average them out. The total acquisition time, however, increases, and, considering 3 repeated acquisitions for each of the $3b$ values, comes identical to the acquisition of signals at 15 different b values. With so many acquired signals one may rather consider fitting those signals with the IVIM/Diffusion model. Eq. (1) can be rewritten as:

$$S(b) = S_{0\text{IVIM}} F_{\text{IVIM}}(b) + S_{0\text{diff}} F_{\text{diff}}(b) \quad [3]$$

$S_{0\text{diff}}$ and $S_{0\text{IVIM}}$ are the fractions of pure diffusion and IVIM components to the overall signal, respectively, with $S_{0\text{diff}} = S_0(1 - f_{\text{IVIM}})$ and $S_{0\text{IVIM}} = S_0 f_{\text{IVIM}}$ where f_{IVIM} is the flowing blood volume fraction and S_0 is the overall signal when $b = 0$. $F_{\text{diff}}(b)$ and $F_{\text{IVIM}}(b)$ are, respectively, the diffusion and perfusion-related IVIM signal attenuation as a function of diffusion weighting (b value). It should be noted here that tissue and blood contribute to S_0 with different T_2 and T_1 -weightings, which means that f_{IVIM} values might be misestimated, depending on TE, on the voxel vessel oxygen content and on the field strength B_0 , an issue when comparing literature results (Fournet et al., 2017; Lemke et al., 2010).

With the pseudo-diffusion model introduced above the expression for $F_{\text{IVIM}}(b)$ is simply:

$$F_{\text{IVIM}}(b) = \exp[-b(D_b + D^*)] \quad [4]$$

As for the diffusion component a common model is the mono-exponential model:

$$F_{\text{diff}}(b) = \exp(-bD) \quad [5]$$

where D is the diffusion coefficient of water in the tissue. This model assumes diffusion is Gaussian (free), an important limitation which can be a source of errors in the estimation of IVIM parameters (see below). Using those two basic models, Eq. (3) takes the shape of the classical biexponential model for IVIM and diffusion:

$$S(b)/S_0 = f_{\text{IVIM}} \exp[-b(D_b + D^*)] + (1 - f_{\text{IVIM}}) \exp(-bD) \quad [6]$$

With a dataset comprising signals acquired at multiple b values one may get estimates of S_0 , F_{IVIM} , D^* (usually D_b is included in D^* , but might be estimated (Funck et al., 2017)) and D by fitting the signal with Eq. (6). However, the fitting process is known to be sensitive to noise and may lead to erroneous or inaccurate parameter estimates if the number of acquired signals is not very large compared to the number of parameters to estimate. Noticing that the IVIM components vanishes at some point when b increases given that the pseudo diffusion coefficient, D^* , is much higher than the water molecular diffusion in tissues, D , a popular and elegant approach is to split the signal in two parts and switch to a 2-step fitting process, first fitting the experimental data for high b -values (above $200\text{--}600 \text{ s/mm}^2$) with the diffusion model for $F_{\text{diff}}(b)$ and then fitting the residual signal after removing the diffusion component at low b values (Iima et al., 2015) with the IVIM model $F_{\text{IVIM}}(b)$.

The question which immediately comes to mind is then to determine the threshold b value which separates the pure diffusion part and the IVIM/diffusion mixed part. Unfortunately, there is no single response, as this threshold value depends on the parameters one has to estimate, f_{IVIM} , D^* and D . Globally, however, one may distinguish two classes of tissues. In the normal brain f_{IVIM} , is less than 5% and D is around $0.002 \text{ mm}^2/\text{s}$, so

that the IVIM component accounts for less than 0.1% of the signal for $b > 200 \text{ s/mm}^2$. In body tissues, however, f_{IVIM} values as high as 20% are not uncommon while D may be on the order of $0.001 \text{ mm}^2/\text{s}$, so that the IVIM component at $b = 400 \text{ s/mm}^2$ may still be around a few %, so that higher threshold b values might be required.

Clearly, the b value threshold should be chosen according to the expected level of perfusion (low in the brain, higher in the body) and the overall signal:noise ratio of the data.

In summary, there is no consensus, yet, on the best processing approach of IVIM data. There is an extensive literature investigating the pros and cons of fitting algorithms, simultaneous or multi-step (Lemke et al., 2011; Barbieri et al., 2016), as well as other methods, such as the Bayesian algorithm (Orton et al., 2014; Wurnig et al., 2015; Spinner et al., 2017; While, 2017) or an adaptive thresholding approach (Wurnig et al., 2015), which are out of the scope of this introductory review.

Non-gaussian diffusion

In all cases, an accurate estimation of the IVIM parameters first requires proper handling of the diffusion component within the IVIM/diffusion MRI signals which account generally for more than 90% of the total signal at low b values. Although the ADC concept has been (and still is) extremely useful, it is based on the assumption of free, Gaussian, diffusion. It has been well established, however, that the diffusion process in tissues is not Gaussian, as the semilog plot of the signal decay, F_{diff} , in biological tissues exhibits a curvature not predicted by Eq. (5) (Iima and Le Bihan, 2016) (Fig. 5). Several models have been suggested to empirically handle this non-Gaussian behavior, such as the polynomial or Kurtosis model (Chabert et al., 2004) (also called Diffusion Kurtosis Imaging, DKI (Jensen et al., 2005)), the biexponential model (Mulkern et al., 2009), the statistical model (Yablonskiy et al., 2003), the stretched exponential model (Bennett et al., 2003), and others (Hall and Barrick, 2008; Zhou et al., 2010) with various success, depending on the context and the tissues under examination. With the kurtosis model one has:

$$F_{\text{diff}} \approx \exp[-b\text{ADC}_0 + (b.\text{ADC}_0)^2 K/6] \quad [7]$$

ADC_0 is the virtual ADC which would be obtained when b approaches 0. The dimensionless coefficient K (kurtosis) characterizes the degree of deviation of the signal behavior from a mono-exponential decay ($K = 0$ when the diffusion driven molecular displacements obey a Gaussian law), a marker of the heterogeneity of the diffusion environment. Hence, Eq. (6) now changes to:

$$S(b)/S_0 = f_{\text{IVIM}} \exp[-b(D_b + D^*)] + (1 - f_{\text{IVIM}}) \exp[-b\text{ADC}_0 + (b.\text{ADC}_0)^2 K/6] \quad [8]$$

An important methodological consequence is that the use of Eq. (5) to fit the diffusion component of the signal above the b value threshold will introduce a significant bias to the estimated perfusion parameters: Fitting the curved diffusion signal attenuation with a straight line (in log plots) according to Eq. (5) results in an artifactual IVIM effect, as acquired data points at low b values will automatically appear above the fitted diffusion signal decay (Fig. 5). The perfusion fraction, f_{IVIM} , will, thus, be *overestimated*. Furthermore, the shape of the residual signal decay at low b values will appear close to an exponential, mimicking Eq. (3), which would be misleading (D^* values would be overestimated as well).

Conversely, ignoring the IVIM component at low b values will lead to an overestimation of kurtosis value when fitting signals with Eq. (8) in one single step. More generally, one should be aware that the Kurtosis model is only one possible model to handle non-gaussian diffusion in $F_{\text{diff}}(b)$, which implies that it is not a perfect model. The kurtosis model is known to fail at very high b values or when the Kurtosis parameter is high (a practical limit is that the triple product $\text{ADC}_0.K.b$ must be smaller than 3). This is an important issue to keep in mind, as any imperfection in fitting the diffusion part of the signal will lead to artifactual IVIM effects and a misestimation (generally an overestimation) of IVIM parameters.

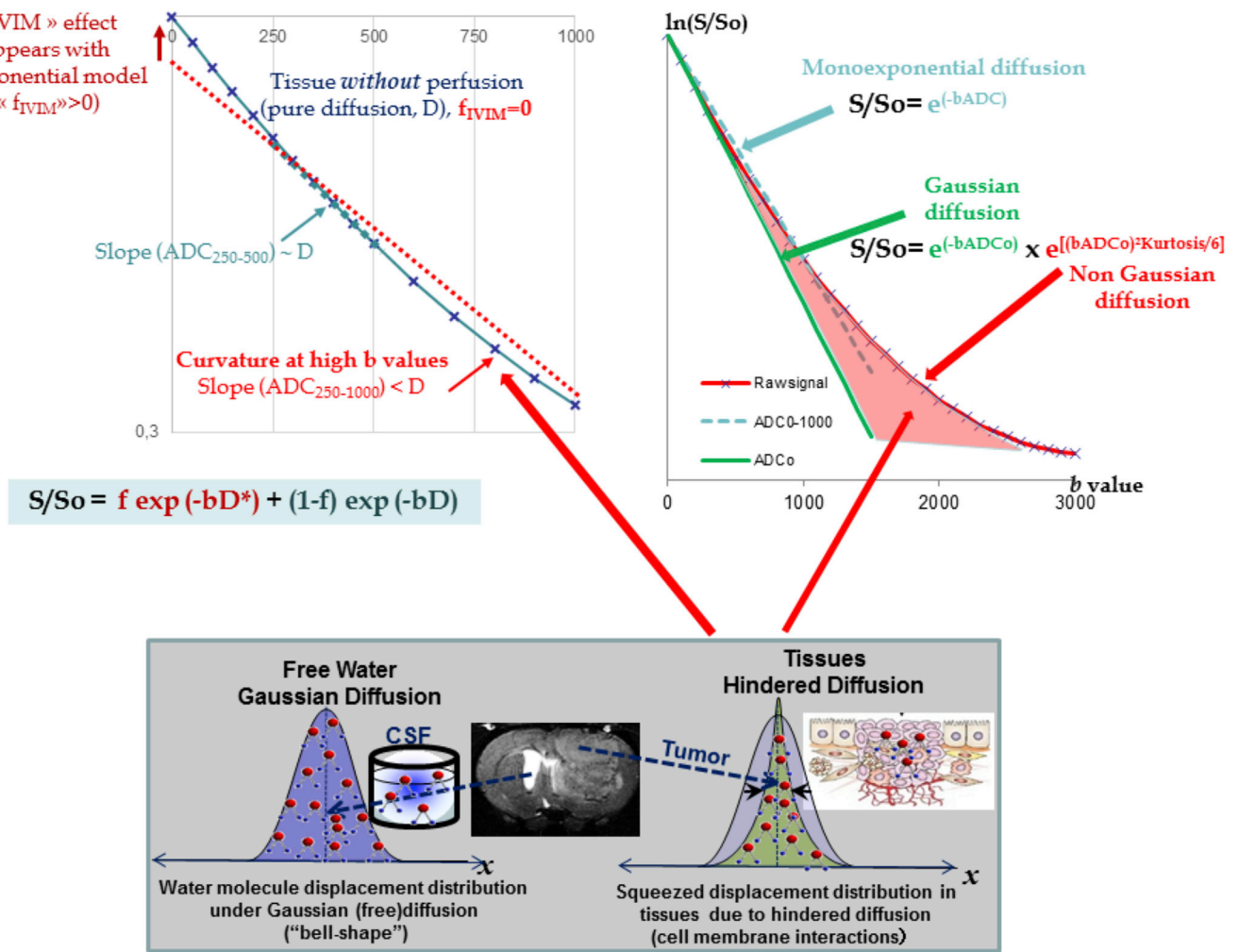


Fig. 5. Non-gaussian diffusion.

Failing to take into account non-Gaussian diffusion effects might lead to erroneous f_{IVIM} and D^* parameter estimates (overestimation), as shown in Fig. 5 in a tissue model without perfusion. Non-Gaussian diffusion which becomes visible at high b values originates from the interaction of water diffusing molecules with obstacles, such as cell membranes, and results in a curvature of the signal attenuation. Modeling the tissue diffusion component with a monoexponential model (such as the ADC) underestimates genuine diffusion ($ADC < D$) when signal at high b values is included, which, in turns, create an artifactual IVIM effect (left). Non-Gaussian diffusion must be properly handled using adequate models, such as the Kurtosis model to avoid such erroneous IVIM effects.

Rician noise

Another important issue to get correct estimate of IVIM parameters is to properly handle noise effects. A particular source of systematic error results from the non-Gaussian nature of the noise in magnitude reconstructed images, resulting in a systematic shift from a noise-free signal (Henkelman, 1985; Gudbjartsson and Patz, 1995). This source of error is particularly prominent at high b values for which the signal/noise ratio (SNR) becomes low. The main effect of such noise is that it may mimic a curvature in the diffusion signal attenuation plot (Fig. 6): At high b values, when SNR becomes low, the signal reaches a “noise floor” and does not get to 0. The signal attenuation appears curved, even for mono-exponential diffusion, and fitting signals with any diffusion model will give erroneous values (e.g., underestimation of ADC, overestimation of kurtosis). As the diffusion component of the signal will not be estimated properly, the perfusion component, which is very sensitive to such errors, will, in turn, be affected, with an underestimation of f_{IVIM} which can even become “negative”. It is thus particularly important to correct for this noise bias all IVIM MRI data, especially when using high b values. Unfortunately, the retrieval of true signal values from noise corrupted data is far from trivial, both theoretically and practically (Gudbjartsson and Patz, 1995; Sijbers et al., 1998). Furthermore, with the use of

phased-array coils instead of single coils the noise structure becomes even more complex (non-central chi square distribution) (Brion et al., 2011; Constantinides et al., 1997; Aja-Fernández et al., 2011; André et al., 2014), and non-stationary with parallel imaging methods, because of the correlation between receiving channels and the under sampling of k -space. Noise correction becomes more problematic, often requiring a large amount of repeated measurements or long computation times.

We recently introduced a simplified procedure where a Noise Correction Factor is experimentally obtained through a phantom calibration process relying on the diffusion MRI signal property itself (Iima et al., 2015). The Noise Correction Factor, NCF, is a parameter which characterizes the “intrinsic” noise contribution from the image acquisition setup (depending on the coils, the MRI sequence parameters, etc.). To illustrate the importance of the effect of noise removal in tissues with high ADC_0 values we provide an example taken in a benign lesion. If noise correction is not applied one finds a high K value and a very high ADC_0 value (Fig. 6). Using such erroneous parameter estimates would result to an estimated signal lower than the measured signal at low b values (see inset), which would mimic a non-perfused tissue (f_{IVIM} could even become negative, a physical non-sense). After noise correction is properly applied the curvature is much reduced and the signal decay close to a straight line: K becomes close to 0 and ADC_0 decreases. The

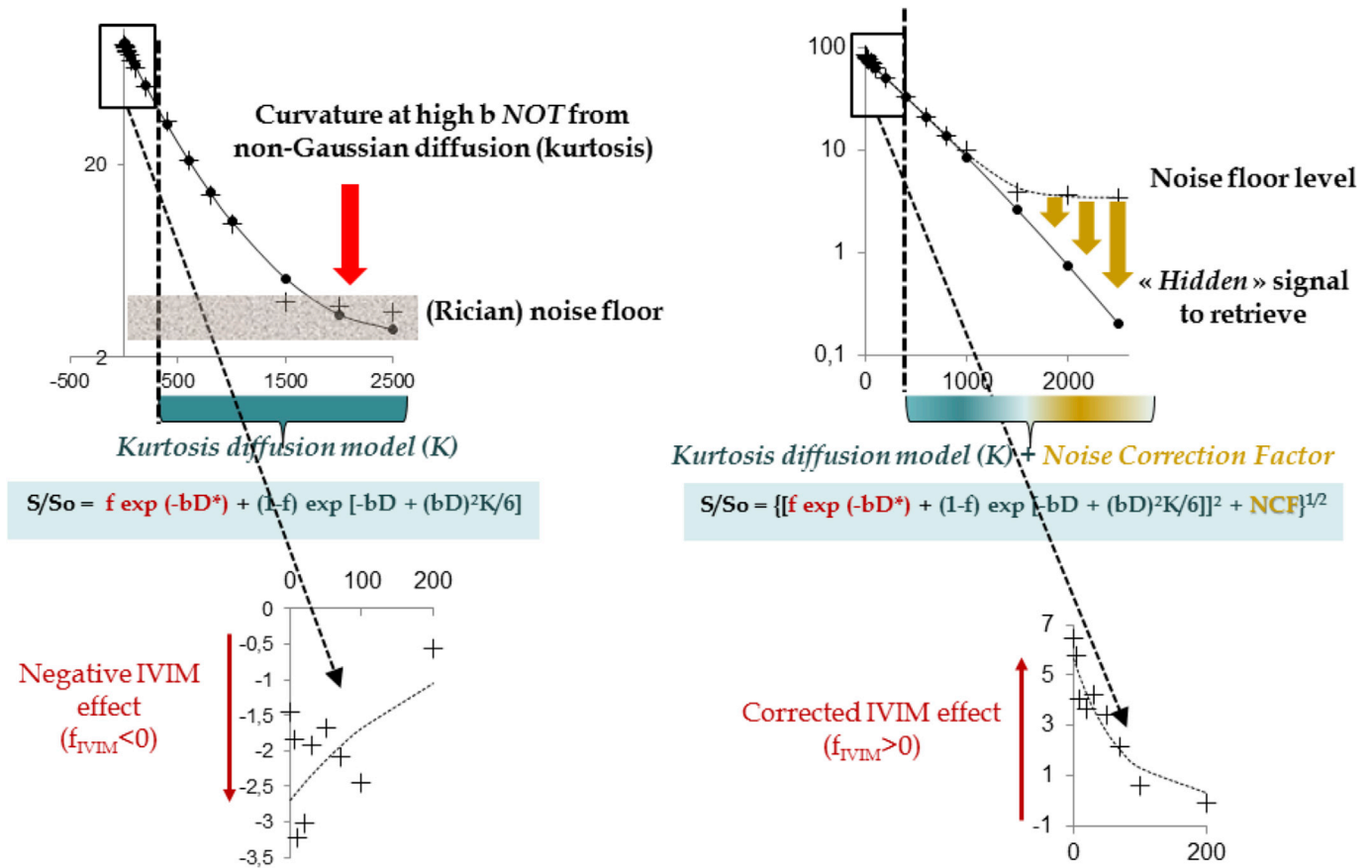


Fig. 6. Effect of Rician noise of IVIM parameters estimates.

At high b values the signal becomes low and may reach the Rician noise floor (the mean of which is not zero), resulting in a curvature of the signal decay, not to be confounded with the curvature produced by non-gaussian diffusion. Failing to remove the noise contribution to the signal amplitude leads to an overestimation of non-Gaussian diffusion (eg, K parameter), which in turn results in an underestimation of f_{IVIM} which can even become negative.

estimated signal at low b values (insert) remains higher than the measured signal, and the estimated f_{IVIM} value is positive, as expected.

Importantly, although non-Gaussian diffusion and noise effects affect signals acquired at high b values, the impact is seen at low b values, as IVIM effects are small. Although it might appear counterintuitive, a proper estimation of diffusion and IVIM parameters, as shown in Figs. 5 and 6 (Iima et al., 2015), might require the inclusion of high b values signals, not only signal acquired at moderate b values (less than 1000 s/mm^2), as often found in the literature.

Signal spoiling

Another source of errors in estimating IVIM parameters is the presence of erratic signals. Spin-echo signals are formed when 90° and 180° radiofrequency pulses are used sequentially. Unfortunately, if those pulses are not perfectly calibrated, spurious signals are generated, such as FIDs following imperfect 180° pulses or stimulated echoes considering the multiple pulses used for multislice acquisitions. Those signals add up to the spin-echo signals, but do not share the IVIM/diffusion encoding of the main spin-echo signals, leading to errors when fitting the overall signals with the IVIM/diffusion model. Pulse imperfections are unavoidable, resulting from inhomogeneities in the B1 field generated by coils, poor shimming or errors in resonance frequencies determination. Generally, those unwanted signals are suppressed with the use of so-called crusher or spoiler gradient pulses placed on each side of the 180° pulses or after each slice readout signal. Those spoiler pulses, however, obviously act as IVIM/diffusion encoding gradients and must be taken into account when calculating b values, which is clearly

unfavorable for IVIM, as the “ $b = 0$ value” is never reachable in the presence of spoiler gradients (or else gradient pulses used for MRI spatial encoding). Obviously, the lowest achievable b values highly depend on each vendor MRI hardware and software. Minimum, values as high as $10\text{--}15$ or even around 50 s/mm^2 are not uncommon, as instabilities in gradient amplifiers may also render low b values unreliable. Conversely, gradient pulses used for diffusion encoding act as spoiler pulses which means that signals acquired with sufficient diffusion encoding are immune from artifacts created by those unwanted signals, while signals at low b values carrying the perfusion IVIM information are not.

Models

Link with capillary architecture and blood flow

The IVIM exponential model used for Eqs. (1) and (3) assumes that flowing blood water changes vessels many times water in randomly oriented capillaries (at voxel level) during the diffusion encoding time, mimicking a collective random walk (“pseudo-diffusion”) (Fig. 1). Overall, there is an empirical consensus that this mono-exponential IVIM model is appropriate to fit data for clinical application studies, as IVIM/diffusion encoding times remain long given the limited capacity of clinical systems gradient hardware. However, this model might not be accurate when the encoding time becomes short or blood velocity is slow or else capillary segments are long. In those conditions blood may remain in single, straight capillary segments during the entire encoding time. If those segments are, nonetheless, randomly oriented over 4π in 3D space the signal attenuation can be modeled as a sinc function (Le Bihan et al.,

1988; Le Bihan, 1990) (Fig. 7):

$$F_{IVIM}(c) = \exp(-bD_b) \text{sinc}(cv) \quad [9]$$

where c is another pulse gradient factor, similar to the b factor. In the case of a pure pulsed-gradient spin-echo sequence with 2 pulses of length δ separated by a time interval Δ one has $c=(b\Delta)^{1/2}$ when $\delta \ll \Delta$. Within this regimen one may also define a pseudo-diffusion coefficient, D^* , by calculating the Taylor expansion limited to the first orders of $F_{IVIM}(c)$, as $D^* = v^2 c^2 / (6b)$ (Le Bihan, 1990). D^* depends on the capillary blood velocity, but no longer depends on the capillary segment length, l , as spins never get to probe the entire capillary segments. Noticeably, this sinc behavior has never been reported experimentally, even at short diffusion times. It can be shown that when blood velocities, v , follow a Gaussian distribution in the capillary network, or when blood flow changes at least 3 times direction during the encoding time $F_{IVIM}(c)$ becomes exponential anyway (Fournet et al., 2017) (Fig. 7).

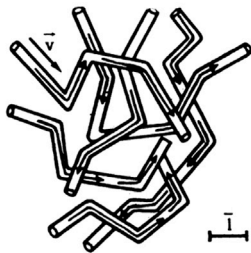
Other models have been proposed to handle intermediate regimens between the monoexponential and sinc IVIM models, taking into account the existence of several vessel functional pools. For instance, Kennan et al. (1994) have introduced a model based on a velocity autocorrelation function. Arguing that the Gaussian phase approximation assumed by Kennan et al. is invalid in some cases, Wetscherek et al. (2015)

introduced another model based on normalized phase distributions. These two models assume that only flow in capillaries contributes to the IVIM signal. Noticing some disagreement between experimental data and the standard mono-exponential model, other authors have suggested models which take into account not only capillaries, but all types of vessels (Henkelman et al., 1994; Duong and Kim, 2000). We recently introduced a bi-exponential IVIM model (not to be confounded with the bi-exponential model used sometimes to separate diffusion and IVIM effects), accounting for two different vascular pools with different blood velocities and geometries, as an alternative to the mono-exponential model (Fournet et al., 2017). This bi-exponential model fits the experimental data better than the standard mono-exponential model at short diffusion times.

Link with classical perfusion parameters

An interesting issue is to establish whether a bridge can be established between the IVIM parameters, f_{IVIM} and D^* , and those which have been used with classical perfusion measurements (Henkelman, 1990; Le Bihan and Turner, 1992), based on the delivery of tracers, as with PET or SPECT. Classical perfusion parameters are, for instance, the blood volume, BV, the blood flow, BF, and the mean transit time, MTT.

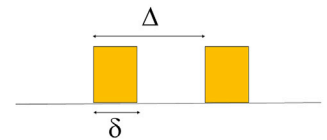
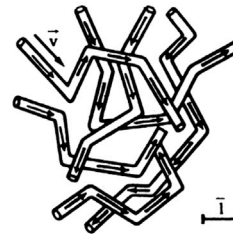
Exponential (pseudo diffusion) model



$$S/S_{0_{IVIM}} = f \exp[-b(D^* + D_{blood})]$$

- ✓ ~ Fast flow
- ✓ Short capillary segments
- ✓ Long measurement times (clinical systems)

Sinc model



C : gradient factor
 $c=(b\Delta)^{1/2}$ when $\delta \ll \Delta$
 $\rightarrow D^* \equiv v^2 c^2 / (6b)$

$$S/S_{0_{IVIM}} = f \exp(-bD_{blood}) \text{sinc}(cv)$$

- ✓ ~ Slow flow
- ✓ Long segments
- ✓ Short measurement times (preclinical systems)

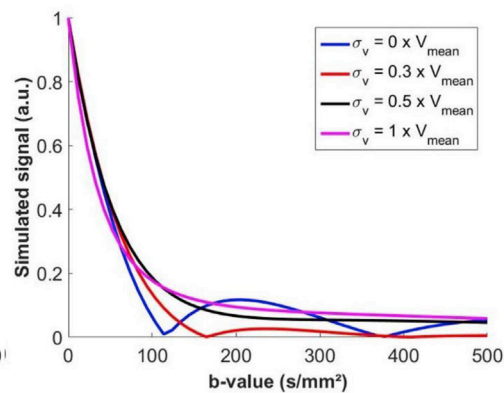
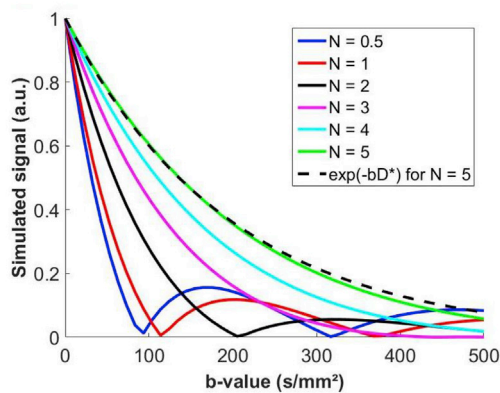


Fig. 7. IVIM blood flow models.

The exponential pseudo-diffusion model assumes blood changes several times direction (capillary segment) during the encoding time. This condition is met when flow is fast enough, capillary segments are not too long and the encoding time is long enough to accommodate those direction changes. In the opposite case where no change in direction occurs the IVIM signal can be modeled by a sinc function if capillary segments are randomly oriented. The transition of a sinc-like model to the exponential model appears when blood flow changes at least 3 times during the encoding time. In all cases, the sinc model may also lead to an exponential model when considering gaussian distributions of blood velocities in the capillary network.

It has been shown that, under some hypotheses, one has (Le Bihan and Turner, 1992):

$$f_{IVIM} = BV/fw \quad [10]$$

$$MTT = L/v = LI/6D^* \quad [11]$$

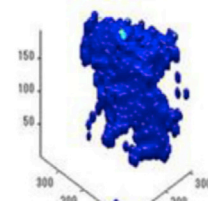
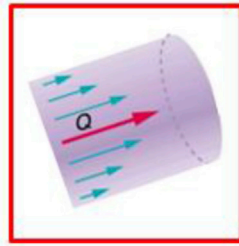
$$BF = (6fw/LI) f_{IVIM} D^* \quad [12]$$

where fw is the MRI-visible water content fraction, L the total capillary length (from artery to vein), MTT the mean transit time, BF the blood flow. As shown from Eq. (11) the element bridging the classical perfusion and IVIM parameters is the capillary network geometry, and more especially two specific lengths characterizing this network: the capillary segment length and the total capillary length. Those quantities are constant for a given tissue, so that relative perfusion or blood flow can potentially be estimated from the product D^*f_{IVIM} . Furthermore, the mean transit time could also be evaluated (at least in a relative manner)

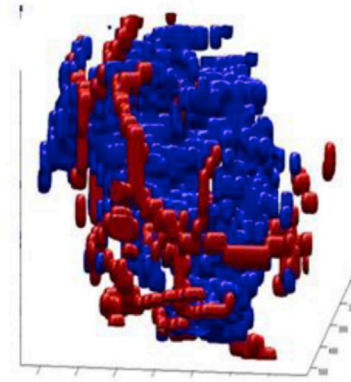
from D^* without the need to estimate an arterial “input function”, which is not a trivial methodological issue, and without the confound of the inclusion of the transit time of blood in the large feeding vessels.

In any case, there is still the need for a deeper insight into the IVIM concept and a clearer understanding of what is seen to fully gain the benefit of the IVIM based perfusion imaging in the clinical setting. The flowing blood fraction, f_{IVIM} , appears correlated with vessel density (Iima et al., 2014; Lee et al., 2014), and recent studies have shown a correlation between f_{IVIM} and CBV (Cerebral Blood Volume) derived from DSC (Dynamic Susceptibility Contrast) MRI in gliomas (Federau et al., 2014; Kim et al., 2014), or DCE (Dynamic Contrast-enhanced) derived parameters in renal tumors (Chandarana et al., 2012), head and neck tumors (Fujima et al., 2014), or breast tumors. But other studies failed to observe such a correlation (Bisdas et al., 2014). One also has to keep in mind that IVIM imaging has a differential sensitivity to vessel sizes, according to the range of b values which are used, but is sensitive to all randomly flowing

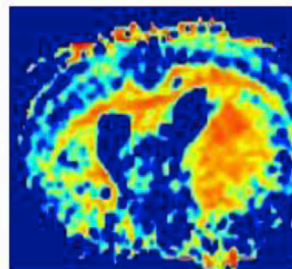
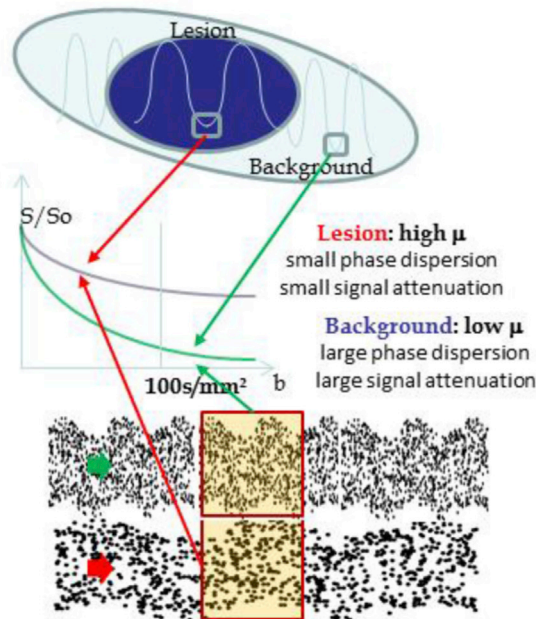
A - IVIM angiography



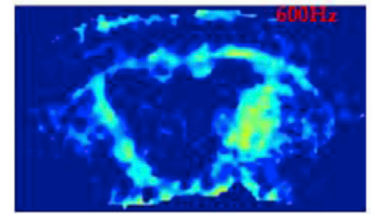
Breast normal tissue



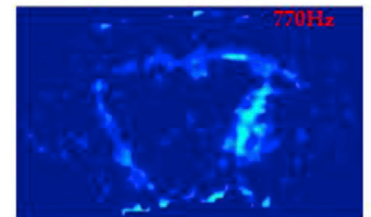
B - IVIM virtual MR elastography



350Hz



600Hz



770Hz

Fig. 8. Other IVIM MRI applications.

A- The spatial distribution of blood velocities in vessels also results in an IVIM effect which can be used to identify voxels containing blood vessels and produce IVIM based angiograms (here is a normal breast) without the need for contrast agents.

B- Mechanical vibrations used for MR elastography also induce phase distributions in each tissue voxel and an IVIM effect when considering the amplitude of the signal. This IVIM effect will be larger in normal tissues than in lesions presenting higher elasticity values, μ , and IVIM MRI could be used, potentially, to estimate those elasticity values. Conversely, if those elasticity values are known (they can be directly derived from diffusion maps, without the need for using mechanical vibrations) virtual IVIM elastographic images can be generated, producing a new kind of contrast which would depend on the combinations of vibration frequencies or amplitudes, as shown here is a model of brain tumor with cells migrating along white matter tracks.

blood in each voxel. Direct comparison with other methods, such as Arterial Spin Labelling (ASL), should remain cautious, as ASL monitors only the transit of blood which has been labeled outside of the voxels, while IVIM reflects all randomly flowing blood in each voxel.

Non perfusion-driven IVIM MRI

IVIM MRI is sensitive to any fluid flow, not only blood, as long as there is an intravoxel distribution. In the brain CSF flow is clearly visible on IVIM images (Le Bihan et al., 1986) and IVIM MRI has been proposed as a CSF flow mapping approach. On the other hand, this sensitivity might also be a confound when evaluating perfusion in the brain cortex if is included as a partial volume effect. CSF suppression techniques may alleviate this pitfall. In other organs, such as the kidneys IVIM MRI may be used to investigate vascular and tubular flow, although they may be difficult to disentangle (Notohamiprodjo et al., 2015). Active transport resulting from glandular secretion (breast ducts, salivary glands and pancreas) may also be explored in addition to microcapillary perfusion.

Beside random capillaries blood flow may also experience incoherent intravoxel dephasing in larger vessels, considering that laminar flow (or even more turbulent flow) leads to a distribution of velocities within the vessel lumen and to an IVIM signal attenuation which could be much larger than the perfusion-driven IVIM effect. This feature can be successfully exploited to identify vessel containing voxels and generate IVIM 3D angiograms without the need for contrast agents (Fig. 8: Angio IVIM).

Another emerging field of application is IVIM/diffusion virtual MR Elastography (dMRE). With standard MRE propagating shear waves through tissues lead to microscopic tissue displacements resulting in phase shifts in the presence of magnetic gradient pulses, which can be exploited to estimate tissue shear stiffness. Tissue elasticity is an interesting parameter, as it has been shown, for instance, that the degree of liver fibrosis could be derived from elasticity measurements (Morisaka et al., 2017). Recently, it has been suggested that tissue shear stiffness (in kPa) could be directly obtained from diffusion MRI without the need to use any mechanical vibration device (Le Bihan et al., 2017). This is possible due to a striking relationship which has been revealed, at least in the liver, between tissue elasticity and tissue water diffusion. This correlation might not be surprising as both relate, although in a different way, to tissue microstructure, but its nature still remains to be investigated and modeled. On the other hand, mechanically-induced phase shifts induced by standard MRE are spatially distributed and results in a phase dispersion in each voxel and an amplitude signal attenuation, that is an IVIM effect (Glaser et al., 2003). The degree of attenuation in those IVIM images would depend on the tissue elasticity and on the choice of acquisition parameters (mainly IVIM b value, vibration frequency and amplitude of the propagating shear waves), creating a new kind of contrast to highlight lesions which are most often associated with a high stiffness. This elasticity-driven IVIM approach, using standard MRE, is challenging, though, as the wave amplitude dampens very quickly when waves penetrate tissues. However, this elasticity-driven IVIM contrast can be emulated *virtually* once the tissue elasticity is known, which can be obtained directly from diffusion MRI without using any mechanical vibration (Le Bihan et al., 2017). This new elasticity-driven IVIM contrast can be emulated for any ranges of virtual vibration frequencies and amplitudes not limited by MRE or MRI hardware capacities, acting as a sort of post-processing filter and revealing tissue details not readily visible with MRE or diffusion MRI (Fig. 8).

Conclusion

Intravoxel Incoherent Motion (IVIM) refers to translational movements which within a given voxel and during the measurement time present a distribution of speeds in orientation and/or amplitude. Although molecular diffusion is the main course of IVIM other types of movements, such as blood microcirculation in the capillary network (perfusion) or shear wave propagation in tissues (elastography), giving to

IVIM MRI a large potential for clinical applications. Especially, IVIM-based perfusion MRI, which has recently received FDA clearance, can provide information on tissue microcirculation and blood flow in addition to information on tissue microstructure from diffusion MRI using the same MRI sequence and without the need for contrast agents. Hence, the potential of IVIM-based perfusion MRI for clinical applications, especially oncology, is rapidly extending. Work remains to fully characterize and model the effects of blood flow at different spatial and temporal scales on the overall IVIM signal, but it appears that a monoexponential decay with the b values remains appropriate in most case. Optimization of IVIM/diffusion data processing pipelines requires attention, given the small range of the flowing blood volume in most tissues. Especially, non-Gaussian diffusion behavior and Rician noise might significantly impact IVIM parameters estimation if not properly accounted for, although such effects are visible mainly in data acquired at high b values.

References

- Aja-Fernández, S., Tristán-Vega, A., Hoge, W.S., 2011. Statistical noise analysis in GRAPPA using a parametrized noncentral chi approximation model. *MRM* 65, 1195–1206.
- Anderson, S.W., Barry, B., Soto, J., Ozonoff, A., O'Brien, M., Jara, H., 2014. Characterizing non-gaussian, high b -value diffusion in liver fibrosis: stretched exponential and diffusional kurtosis modeling. *JMRI* 39 (4), 827–834.
- André, E.D., Grinberg, F., Farrher, E., et al., 2014. Influence of noise correction on intra- and inter-subject variability of quantitative metrics in diffusion kurtosis imaging. *PLoS One* 9, e94531.
- Andreou, A., Koh, D.M., Collins, D.J., et al., 2013. Measurement reproducibility of perfusion fraction and pseudodiffusion coefficient derived by intravoxel incoherent motion diffusion-weighted MR imaging in normal liver and metastases. *Eur. Radiol.* 23, 428–434.
- Barbieri, S., Donati, O.F., Froehlich, J.M., Thoeny, H.C., 2016. Impact of the calculation algorithm on biexponential fitting of diffusion-weighted MRI in upper abdominal organs. *MRM* 75 (5), 2175–2184.
- Van Beers, B.E., 2014. Science to practice: can we diagnose nonalcoholic steatohepatitis with intravoxel incoherent motion diffusion-weighted MR imaging? *Radiology* 270 (1), 1–2.
- Belliveau, J.W., Kennedy, D.N., McKinstry, R.C., Burchbinder, B.R., Weisskoff, R.M., Cohen, M.S., Vevea, J.M., Brady, T.J., Rosen, B.R., Buchbinder, B.R., 1991. Functional mapping of the human visual cortex by magnetic resonance imaging. *Science* 254, 716–719.
- Bennett, K.M., Schmainda, K.M., Bennett, R.T., Rowe, D.B., Lu, H., Hyde, J.S., 2003. Characterization of continuously distributed cortical water diffusion rates with a stretched-exponential model. *MRM* 50 (4), 727–734.
- Le Bihan, D., 1990. Magnetic resonance imaging of perfusion. *MRM* 14, 283–292.
- Le Bihan, D., Turner, R., 1992. The capillary network: a link between IVIM and classical perfusion. *MRM* 27, 171–178.
- Le Bihan, D., Breton, E., Lallemand, D., Grenier, P., Cabanis, E., Laval Jeantet, M., 1986. MR Imaging of intravoxel incoherent motions: application to diffusion and perfusion in neurologic disorders. *Radiology* 161, 401–407.
- Le Bihan, D., Breton, E., Lallemand, D., Aubin, M.L., Vignaud, J., Laval-Jeantet, M., 1988. Separation of diffusion and perfusion in intravoxel incoherent motion MR imaging. *Radiology* 168, 497–505.
- Le Bihan, D., Ichikawa, S., Motosugu, U., 2017. Diffusion and Intravoxel Incoherent Motion (IVIM) MRI based virtual elastography: a hypothesis generating study in the liver. *Radiology* 285 (2), 609–619.
- Bisdas, S., Koh, T.S., Roder, C., Braun, C., Schittenhelm, J., Ernemann, U., Klose, U., 2013. Intravoxel incoherent motion diffusion-weighted MR imaging of gliomas: feasibility of the method and initial results. *Neuroradiology* 55 (10), 1189–1196.
- Bisdas, S., Braun, C., Skardelly, M., Schittenhelm, J., Teo, T.H., Thng, C.H., Klose, U., Koh, T.S., 2014. Correlative assessment of tumor microcirculation using contrast-enhanced perfusion MRI and intravoxel incoherent motion diffusion-weighted MRI: is there a link between them? *NMR Biomed.* 27 (10), 1184–1191.
- Bokacheva, L., Kaplan, J.B., Giri, D.D., Patil, S., Gnanasigamani, M., Nyman, C.G., Deasy, J.O., Morris, E.A., Thakur, S.B., 2014. Intravoxel incoherent motion diffusion-weighted MRI at 3.0T differentiates malignant breast lesions from benign lesions and breast parenchyma. *JMRI* 40 (4), 813–823.
- Boxerman, J.L., Bandettini, P.A., Kwong, K.K., Baker, J.R., Davis, T.L., Rosen, B.R., Weisskoff, R.M., 1995. The intravascular contribution of fMRI signal change: Monte Carlo modeling and diffusion-weighted studies in vivo. *MRM* 34, 4–10.
- Brion, V., Poupon, C., Riff, O., et al., 2011. Parallel MRI Noise Correction: An Extension of the LMMSE to Non Central χ Distributions. *Medical Image Computing and Computer-Assisted Intervention—MICCAI*. Springer, pp. 226–233.
- Chabert, S., Meca, C., Le Bihan, D., 2004. Relevance of the information about the diffusion distribution in vivo given by kurtosis in q -space imaging. In: *Proceedings of the 12th Annual Meeting of ISMRM*, Kyoto, Japan, p. 1238.
- Chandarana, H., Lee, V.S., Hecht, E., Taouli, B., Sigmund, E.E., 2011. Comparison of biexponential and monoexponential model of diffusion weighted imaging in evaluation of renal lesions: preliminary experience. *Invest. Radiol.* 46 (5), 285–291.

- Chandarana, H., Kang, S.K., Wong, S., et al., 2012. Diffusion-weighted intravoxel incoherent motion imaging of renal tumors with histopathologic correlation. *Invest. Radiol.* 47 (12), 688–696.
- Chow, A.M., Gao, D.S., Fan, S.J., Qiao, Z., Lee, F.Y., Yang, J., Man, K., Wu, E.X., 2012. Liver fibrosis: an intravoxel incoherent motion (IVIM) study. *JMRI* 36 (1), 159–167.
- Constantinides, C.D., Atalar, E., McVeigh, E.R., 1997. Signal-to-noise measurements in magnitude images from NMR phased arrays. *MRM* 38, 852–857.
- Dixon, W.T., 1988. Separation of diffusion and perfusion in intravoxel incoherent motion MR imaging: a modest proposal with tremendous potential. *Radiology* 168, 566–567.
- Döpfert, J., Lemke, A., Weidner, A., Schad, L.R., Oct 2011. Investigation of prostate cancer using diffusion-weighted intravoxel incoherent motion imaging. *Magn. Reson. Imag.* 29 (8), 1053–1058.
- Duong, T.Q., Kim, S.G., 2000. In vivo MR measurements of regional arterial and venous blood volume fractions in intact rat brain. *MRM* 43, 393–402.
- Duong, T.Q., Yacoub, E., Adriany, G., Hu, X.P., Ugurbil, K., Kim, S.G., 2003. Microvascular BOLD contribution at 4 and 7 T in the human brain: gradient-echo and spin-echo fMRI with suppression of blood effects. *MRM* 49, 1019–1027.
- Dyvorne, H.A., Galea, N., Nevers, T., et al., 2013. Diffusion-weighted imaging of the liver with multiple b values: effect of diffusion gradient polarity and breathing acquisition on image quality and intravoxel incoherent motion parameters—a pilot study. *Radiology* 266, 920–929.
- Federau, C., Meuli, R., O'Brien, K., Maeder, P., Hagmann, P., 2014. Perfusion measurement in brain gliomas with intravoxel incoherent motion MRI. *Am. J. Neuroradiol.* 35 (2), 256–262.
- Fournet, G., Li, J.R., Cerjanic, A.M., Sutton, B.P., Ciobanu, L., Le Bihan, D., 2017. A two-pool model to describe the IVIM cerebral perfusion. *J. Cerebr. Blood Flow Metabol.* 37 (8), 2987–3000.
- Fujima, N., Yoshida, D., Sakashita, T., et al., 2014. Intravoxel incoherent motion diffusion-weighted imaging in head and neck squamous cell carcinoma: assessment of perfusion-related parameters compared to dynamic contrast-enhanced MRI. *Magn. Reson. Imag.* 32 (10), 1206–1213.
- Funck, C., Laun, F.B., Wetscherek, A., Sep 23, 2017. Characterization of the diffusion coefficient of blood. *MRM*. <https://doi.org/10.1002/mrm.26919> [Epub ahead of print] PubMed PMID: 28940621.
- Gaig, B., Sigmund, E.E., Huang, W.C., et al., 2015. Subtype differentiation of renal tumors using voxel-based histogram analysis of intravoxel incoherent motion parameters. *Invest. Radiol.* 50 (3), 144–152.
- Glaser, K.J., Felmlee, J.P., Manduca, A., Ehman, R.L., 2003. Shear stiffness estimation using intravoxel phase dispersion in magnetic resonance elastography. *MRM* 50, 1256–1265.
- Gudbjartsson, H., Patz, S., 1995. The Rician distribution of noisy MRI data. *Magn. Reson. Med.* 34, 910–914.
- Hall, M.G., Barrick, T.R., 2008. From diffusion-weighted MRI to anomalous diffusion imaging. *MRM* 59 (3), 447–455.
- Henkelman, R.M., 1985. Measurement of signal intensities in the presence of noise in MR images. *Med. Phys.* 12, 232–233.
- Henkelman, R.M., 1990. Does IVIM measure classical perfusion? *MRM* 16, 470–475.
- Henkelman, R.M., Neil, J.J., Xiang, Q.S., 1994. A quantitative interpretation of IVIM measurements of vascular perfusion in the rat brain. *MRM* 32, 464–469.
- Ichikawa, S., Motosugi, U., Ichikawa, T., Sano, K., Morisaka, H., Araki, T., 2013. Intravoxel incoherent motion imaging of focal hepatic lesions. *JMRI* 37, 1371–1376.
- Ichikawa, S., Motosugi, U., Ichikawa, T., Sano, K., Morisaka, H., Araki, T., 2013. Intravoxel incoherent motion imaging of the kidney: alterations in diffusion and perfusion in patients with renal dysfunction. *Magn. Reson. Imag.* 31 (3), 414–417.
- Iima, M., Le Bihan, D., 2016. Clinical intravoxel incoherent motion and diffusion MR imaging: past, present, and future. *Radiology* 278, 13–32.
- Iima, M., Kataoka, M., Le Bihan, D., et al., 2013. Potential of perfusion imaging with IVIM MRI on breast cancer. In: *Proceedings ISMRM Annual Meeting*, p. 1814.
- Iima, M., Reynaud, O., Tsurugizawa, T., et al., 2014. Characterization of glioma microcirculation and tissue features using intravoxel incoherent motion magnetic resonance imaging in a rat brain model. *Invest. Radiol.* 49 (7), 485–490.
- Iima, M., Yano, K., Kataoka, M., Umehana, M., Murata, K., Kanao, S., et al., 2015. Quantitative non-Gaussian diffusion and intravoxel incoherent motion magnetic resonance imaging: differentiation of malignant and benign breast lesions. *Invest. Radiol.* 50, 205–211.
- Iima, M., Kataoka, M., Kanao, S., Onishi, N., Kawai, M., Ohashi, A., Sakaguchi, R., Toi, M., Togashi, K., Nov 2, 2017. Intravoxel incoherent motion and quantitative non-gaussian diffusion MR imaging: evaluation of the diagnostic and prognostic value of several markers of malignant and benign breast lesions. *Radiology* 162853. <https://doi.org/10.1148/radiol.2017162853> (Epub ahead of print).
- Jensen, J.H., Helpert, J.A., Ramani, A., Lu, H., Kaczynski, K., 2005. Diffusional kurtosis imaging: the quantification of non-gaussian water diffusion by means of magnetic resonance imaging. *MRM* 53 (6), 1432–1440.
- Jin, T., Zhao, F., Kim, S.G., 2006. Sources of functional apparent diffusion coefficient changes investigated by diffusion-weighted spin-echo fMRI. *MRM* 56, 1283–1292.
- Joo, I., Lee, J.M., Yoon, J.H., Jang, J.J., Han, J.K., Choi, B.I., 2014. Nonalcoholic fatty liver disease: intravoxel incoherent motion diffusion-weighted MR imaging—an experimental study in a rabbit model. *Radiology* 270 (1), 131–140.
- Kanda, T., Ishii, K., Kawaguchi, H., Kitajima, K., Takenaka, D., 2014. High signal intensity in the dentate nucleus and globus pallidus on unenhanced T1-weighted MR images: relationship with increasing cumulative dose of a gadolinium-based contrast material. *Radiology* 270, 834–841.
- Kanda, T., Osawa, M., Oba, H., Toyoda, K., Kotoku, J., Haruyama, T., et al., 2015. High signal intensity in dentate nucleus on unenhanced T1-weighted MR images: association with linear versus macrocyclic gadolinium chelate administration. *Radiology* 275, 803–809.
- Kennan, R.P., Gao, J.H., Zhong, J., Gore, J.C., 1994. A general model of microcirculatory blood flow effects in gradient sensitized MRI. *Med. Phys.* 21, 539–545.
- Kim, T., Kim, S.G., 2006. Quantification of cerebral arterial blood volume using arterial spin labeling with intravoxel incoherent motion-sensitive gradients. *MRM* 55, 1047–1057.
- Kim, H.S., Suh, C.H., Kim, N., Choi, C.G., Kim, S.J., 2014. Histogram analysis of intravoxel incoherent motion for differentiating recurrent tumor from treatment effect in patients with glioblastoma: initial clinical experience. *AJNR* 35 (3), 490–497.
- Koh, D., Scurr, E., Collins, D., et al., 2006. Colorectal hepatic metastases: quantitative measurements using single-shot echo-planar diffusion-weighted MR imaging. *Eur. Radiol.* 16 (9), 1898–1905.
- Koh, D.-M., Collins, D.J., Orton, M.R., 2011. Intravoxel incoherent motion in body diffusion-weighted MRI: reality and challenges. *Am. J. Rev.* 196, 1351–1361.
- Lee, S.P., Silva, A.C., Kim, S.G., 2002. Comparison of diffusion-weighted high-resolution CBF and spin-echo BOLD fMRI at 9.4 T. *MRM* 47, 736–741.
- Lee, H.J., Rha, S.Y., Chung, Y.E., et al., 2014. Tumor perfusion-related parameter of diffusion-weighted magnetic resonance imaging: correlation with histological microvessel density. *MRM* 71 (4), 1554–1558.
- Lee, Y., Lee, S.S., Kim, N., et al., 2015. Intravoxel incoherent motion diffusion-weighted MR imaging of the liver: effect of triggering methods on regional variability and measurement repeatability of quantitative parameters. *Radiology* 274 (2), 405–415.
- Lemke, A., Laun, F.B., Simon, D., Stieltjes, B., Schad, L.R., 2010. An in vivo verification of the intravoxel incoherent motion effect in diffusion-weighted imaging of the abdomen. *MRM* 64 (6), 1580–1585.
- Lemke, A., Stieltjes, B., Schad, L.R., Laun, F.B., 2011. Toward an optimal distribution of b values for intravoxel incoherent motion imaging. *Magn. Reson. Imag.* 29, 766–776.
- Luciani, A., Vignaud, A., Cavet, M., et al., 2008. Liver cirrhosis: intravoxel incoherent motion MR imaging—pilot study 1. *Radiology* 249 (3), 891–899.
- Micheli, C.R., Song, A.W., MacFall, J.R., 2006. Dependence of gradient-echo and spin-echo BOLD fMRI at 4 T on diffusion weighting. *NMR Biomed.* 19, 566–572.
- Morisaka, H., Motosugi, U., Ichikawa, S., Nakazawa, T., Kondo, T., Funayama, S., Matsuda, M., Ichikawa, T., Onishi, H., Oct 14, 2017. Magnetic resonance elastography is as accurate as liver biopsy for liver fibrosis staging. *JMRI*. <https://doi.org/10.1002/jmri.25868> (Epub ahead of print).
- Morvan, D., 1995. In vivo measurement of diffusion and pseudo-diffusion in skeletal muscle at rest and after exercise. *Magn. Reson. Imag.* 13, 193–199.
- Mulkern, R.V., Haker, S.J., Maier, S.E., 2009. On high b diffusion imaging in the human brain: ruminations and experimental insights. *Magn. Reson. Imag.* 27 (8), 1151–1162.
- Neil, J.J., Bosch, C.S., Ackerman, J.J., 1994. An evaluation of the sensitivity of the intravoxel incoherent motion (IVIM) method of blood flow measurement to changes in cerebral blood flow. *MRM* 32, 60–65.
- Notohamidjodjo, M., Chandarana, H., Mikheev, A., et al., 2015. Combined intravoxel incoherent motion and diffusion tensor imaging of renal diffusion and flow anisotropy. *MRM* 73 (4), 1526–1532.
- Ogawa, S., Tank, D.W., Menon, R.S., Ellerman, J.M., Kim, S.G., Merkle, H., Ugurbil, K., 1992. Intrinsic signal changes accompanying sensory stimulation—functional brain mapping with magnetic resonance imaging. *Proc. Natl. Acad. Sci. U. S. A.* 89, 5951–5955.
- Orton, M.R., Collins, D.J., Koh, D.M., Leach, M.O., 2014. Improved intravoxel incoherent motion analysis of diffusion weighted imaging by data driven Bayesian modeling. *MRM* 71 (1), 411–420.
- Patel, J., Sigmund, E.E., Rusinek, H., Oei, M., Babb, J.S., Taouli, B., 2010. Diagnosis of cirrhosis with intravoxel incoherent motion diffusion MRI and dynamic contrast-enhanced MRI alone and in combination: preliminary experience. *JMRI* 31 (3), 589–600.
- Pavlik, C., Rackl, A., Bing, R.J., 1981. Quantitative capillary topography and blood flow in the cerebral cortex of cats: an in-vivo microscopic study. *Brain Res.* 208, 35–58.
- Pickens III, D.R., Jolgren, D.L., Lorenz, C.H., Creasy, J.L., Price, R.R., 1992. Magnetic resonance perfusion/diffusion imaging of the excised dog kidney. *Invest. Radiol.* 27, 287–292.
- Powers, T.A., Lorenz, C.H., Holburn, G.E., Price, R.R., 1991. Renal artery stenosis: in vivo perfusion MR imaging. *Radiology* 178 (2), 543–548.
- Sigmund, E.E., Cho, G.Y., Kim, S., et al., 2011. Intravoxel incoherent motion imaging of tumor microenvironment in locally advanced breast cancer. *Magn. Reson. Med.* 65, 1437–1447.
- Sijbers, J., Den Dekker, A.J., Scheunders, P., et al., 1998. Maximum-likelihood estimation of Rician distribution parameters. *Medical Imaging, IEEE Transactions* 17, 357–361.
- Silva, A.C., Williams, D.S., Koretsky, A.P., 1997. Evidence for the exchange of arterial spin-labeled water with tissue water in rat brain from diffusion-sensitized measurements of perfusion. *MRM* 38, 232–237.
- Song, A.W., Li, T., 2003. Improved spatial localization based on flow-moment-nulled and intra-voxel incoherent motion-weighted fMRI. *NMR Biomed.* 16, 137–143.
- Song, A.W., Wong, E.C., Tan, S.G., Hyde, J.S., 1996. Diffusion weighted fMRI at 1.5 T. *MRM* 35, 155–158.
- Spinner, G.R., von Deuster, C., Tezcan, K.C., Stoeck, C.T., Kozerke, S., 2017. Bayesian intravoxel incoherent motion parameter mapping in the human heart. *J. Cardiovasc. Magn. Reson.* 19 (1), 85.
- Taouli, B., Vilgrain, V., Dumont, E., Daire, J.-L., Fan, B., Menu, Y., 2003. Evaluation of liver diffusion isotropy and characterization of focal hepatic lesions with two single-shot echo-planar MR imaging sequences: prospective study in 66 patients. *Radiology* 226 (1), 71–78.
- Truong, T.K., Song, A.W., 2009. Cortical depth dependence and implications on the neuronal specificity of the functional apparent diffusion coefficient contrast. *Neuroimage* 47 (1), 65–68.

- Turner, R., Le Bihan, D., Maier, J., Vavrek, R., Hedges, L.K., Pekar, J., 1990. Echo-planar imaging of intravoxel incoherent motions. *Radiology* 177, 407–414.
- Wetscherek, A., Stieltjes, B., Laun, F.B., 2015. Flow-compensated intravoxel incoherent motion diffusion imaging. *MRM* 74, 410–419.
- While, P.T., 2017. A comparative simulation study of bayesian fitting approaches to intravoxel incoherent motion modeling in diffusion-weighted MRI. *MRM* 78 (6), 2373–2387.
- Wurnig, M.C., Donati, O.F., Ulbrich, E., Filli, L., Kenkel, D., Thoeny, H.C., Boss, A., 2015. Systematic analysis of the intravoxel incoherent motion threshold separating perfusion and diffusion effects: proposal of a standardized algorithm. *MRM* 74 (5), 1414–1422.
- Yablonskiy, D.A., Bretthorst, G.L., Ackerman, J.J., 2003. Statistical model for diffusion attenuated MR signal. *MRM* 50 (4), 664–669.
- Yamada, I., Aung, W., Himeno, Y., Nakagawa, T., Shibuya, H., 1999. Diffusion coefficients in abdominal organs and hepatic lesions: evaluation with intravoxel incoherent motion echo-planar MR imaging. *Radiology* 210, 617–623.
- Yoon, J.H., Lee, J.M., Yu, M.H., Kiefer, B., Han, J.K., Choi, B.I., 2014. Evaluation of hepatic focal lesions using diffusion-weighted MR imaging: comparison of apparent diffusion coefficient and intravoxel incoherent motion-derived parameters. *JMRI* 39 (2), 276–285.
- Zhou, X.J., Gao, Q., Abdullah, O., Magin, R.L., 2010. Studies of anomalous diffusion in the human brain using fractional order calculus. *MRM* 63 (3), 562–569.
- Van Zijl, P.C.M., Moonen, C.T.W., Faustino, P., Pekar, J., Kaplan, O., Cohen, J.S., 1991. Complete separation of intracellular and extracellular information in NMR spectra of perfused cells by diffusion-weighted spectroscopy. *Proc. Natl. Acad. Sci. U. S. A.* 88, 3228–3232.